Available online at www.sciencedirect.com
SCIENCE DIRECT®
International Journal of Heat and Mass Transfer 47 (2004) 5339–5349
International Journal of HEAT and MASS TRANSFER
www.elsevier.com/locate/ijhmt

Solidification characteristics of rising immiscible oil droplets in coolant

Y. Nakao [a], M. Hishida [a,*], G. Tanaka [a], Y. Shiina [b]

[a] Department of Electronics and Mechanical Engineering, Chiba University, Yayoi-cho, Inage-ku, Chiba-shi 263-8522, Japan
[b] Department of Advanced Nuclear Heat Technology, Oarai Establishment, JAERI 3607, Oarai-machi, Higashi-Ibaraki-gun, Ibaraki-ken 311-1394, Japan

Received 12 July 2003; received in revised form 14 April 2004

Abstract

Solidification characteristics of hexadecane particles injected through a single nozzle into coolants of stagnant pure water, ethylene glycol 30 wt% water solution, and ethylene glycol 50 wt% water solution were investigated. Experimental parameters were varied in the ranges of $22.4 < Re_p < 492$, $8.79 < Pr < 49.9$, $0.0475 < Ste < 0.0741$, and $0.0566 < Fo < 1.66$. The investigation was focused on the solidification phenomena of hexadecane particles in coolants. The present study is summarized in the following. (1) Empirical equation correlating the drag coefficients of hexadecane particles was proposed, and (2) empirical equations correlating the solidification mass fraction of hexadecane particles were proposed for low injection velocity condition and for higher injection velocity condition independently.

Keywords: Solidification; Thermal energy storage; Direct heat exchange; Hexadecane droplets; Nozzle injection

1. Introduction

It is well known that a conventional latent heat storage system has a disadvantage in that the speed of solidification of the phase change material (PCM) decreases with time. This occurs because the thickness of solid-phase PCM layer, through which the heat transfer occurs, increases with time. The solid-phase PCM layer presents an increasing heat transfer resistance between the liquid-phase PCM and the working fluid (thermal energy carrier). This reduces the thermal energy transfer rate from the liquid PCM with time.

To overcome this disadvantage in a conventional latent heat storage system, marked attention has been focused on a direct contact type thermal energy storage system. In a direct contact type system, small droplets of PCM exchange thermal energy with a working fluid. The very small thermal resistance of small-size PCM droplets may make this concept suitable for high-efficiency thermal energy storage systems. This system has the additional advantage of being able to transport high-density thermal energy in the working fluid stream.

Although direct contact heat and mass transfer between liquid droplets and continuous liquid media as well as between solid particles and continuous liquid media have been extensively studied for a wide range of industrial applications [1], limited research has addressed direct contact solidification (freezing) of PCM

* Corresponding author. Tel./fax: +81 43 290 3180.
E-mail address: hishida@faculty.chiba-u.jp (M. Hishida).

0017-9310/$ - see front matter © 2004 Elsevier Ltd. All rights reserved.
doi:10.1016/j.ijheatmasstransfer.2004.05.036

Nomenclature

Bi	Biot number = hd_p/λ_{ps}
Fo	Fourier number = $\lambda_{ps}\Delta H/c_{ps}\rho d_p^2 U_p$
g	acceleration of gravity [m/s^2]
h	heat transfer coefficient [W/m^2 K]
H	enthalpy [J]
L	latent heat [J/kg]
Nu	Nusselt number = hd_p/λ_c
Pr	Prandtl number = $c_c\rho_c v_c/\lambda_c$
Re_p	Reynolds number = $U_p d_p/v_c$
Ste	Stefan number = $c_{ps}(T_m - T_c)/L$
t_f	time required for a particle to ascend from starting height of solidification to top surface of coolant [s]
U	velocity [m/s]

Greek symbols

γ	solidification ratio
λ	thermal conductivity [W/m K]
μ	viscosity [Pa s]
v	dynamic viscosity [m^2/s]
ρ	density [kg/m^3]

Subscripts

c	coolant
i	inner surface of a solidifying particle
l	liquid phase
m	melting temperature of hexadecane
n	nozzle
o	outer surface of a particle
p	particle
s	solid phase
t	terminal
total	total solid and liquid phase

droplets moving in a liquid coolant. Inaba et al. [2–4] investigated direct contact solidification of tetradecane droplets ascending in ethylene glycol 30 wt% water solution (hereafter, EG 30 wt% water solution). They experimentally investigated the effects of the injection velocity and temperature of tetradecane (PCM), and the flow velocity and temperature of EG 30 wt% water solution (coolant) on the solidification rate of tetradecane droplets. The group also theoretically investigated the ascending velocity, temperature profile, and solidification process of the droplets. They calculated the ascending velocity of tetradecane droplets injected into EG 30 wt% water solution using the mathematical model proposed by Basset, Boussinesq, and Ossen in Hinze [5]. The temperature distribution and solidification rate of the tetradecane droplets based on a one-dimensional heat transfer model were also calculated by the group. Based on their experimental and theoretical studies, they proposed empirical equations for the solidification rate and overall heat transfer coefficient of tetradecane droplets. Inaba et al. [6] also investigated the direct contact freezing of meso-erythritol droplets injected into stagnant silicone oil and proposed empirical equations for the overall heat transfer coefficient between meso-erythritol droplets and silicone oil.

However, further studies are necessary to determine if the proposed equations for the solidification rate and overall heat transfer coefficient can be applied to systems other than that used by Inaba et al. This is important because their experimental studies were limited mainly to a system of tetradecane droplets injected into EG 30 wt% water solution, and the solidification rates were measured only at a position 160 cm above the injection nozzle.

In the present study, we experimentally examined direct contact freezing of hexadecane droplets ascending in stagnant water, EG 30 wt% water solution, and EG 50 wt% water solution. In our experiments, we measured the solidification mass fraction at three height above an injection nozzle.

Direct heat transfer between hexadecane droplets and a surrounding coolant liquid occurs in two steps. In the first step, liquid hexadecane droplets released from an injection nozzle exchange heat with the surrounding liquid coolant. When the surface temperature of a liquid droplet reaches its solidification temperature, a thin solidified layer of hexadecane begins to envelop the hexadecane droplet. In this first cooling step, which is terminated by the start of solidification, the sensible heat of the droplet is dissipated into the coolant by convective heat transfer inside as well as outside the liquid droplet.

In the second cooling step, which is initiated by the start of solidification of the hexadecane particle surface, the latent heat of solidification released by freezing is transferred by conductive heat transfer through the solid enveloping layer forming on the particle and is transferred by convective heat transfer from the particle surface to the coolant. At this time, the sensible heat transfer rate from liquid PCM contained in the core of droplet is small compared to the latent heat of solidification transfer rate; thus, the heat transfer in the liquid core is of little significance.

This study focuses on the solidification phenomena in the second step of the heat transfer process, since the

first step, direct heat transfer between liquid droplets and continuous medium, has been extensively studied for a wide range of industrial applications.

2. Experimental apparatus and methods

In this study, hexadecane was used as the PCM and pure water, ethylene glycol 30 wt% water solution (EG 30 wt% water solution), and ethylene glycol 50 wt% water solution (EG 50 wt% water solution) were used as coolant. Table 1 shows physical properties of hexadecane and coolants used in the present paper.

Fig. 1 shows the experimental heat exchange apparatus consisting of a coolant tank (heat exchanger), coolant temperature control unit, and droplet-launching unit. The coolant tank is made of 10-mm-thick acrylic plates. Its cross section is 16×16 cm and its height is 260 cm. Coolant is supplied to the tank from the coolant temperature control unit, which maintains the coolant at a fixed temperature until the start of an experiment. The valves in the temperature control unit are closed to prevent a circulation flow from the tank to temperature control unit during the experiments. A nozzle situated at the bottom of tank injects hexadecane droplets into the coolant. The injection nozzle has a 1.0-mm inner diameter, a 2.0-mm outer diameter and a 0.5-mm length. The temperature of the injected liquid hexadecane is set at a fixed temperature by the temperature control bath in the droplet-launching unit. In the coolant tank, the hexadecane droplets transfer their heat to the coolant and solidify. Hereafter, we will identify a liquid droplet as a droplet and a completely solidified droplet as a particle. Particle is also used to indicate a partly solidified particle, i.e., one containing some liquid. The coolant temperature is measured by five Type K thermocouples placed in a corner of the coolant tank at 50-cm intervals in height. The deviation of temperature measured by the five thermocouples is within 0.5 °C. Also, a Type K thermocouple is located in the injection nozzle to measure

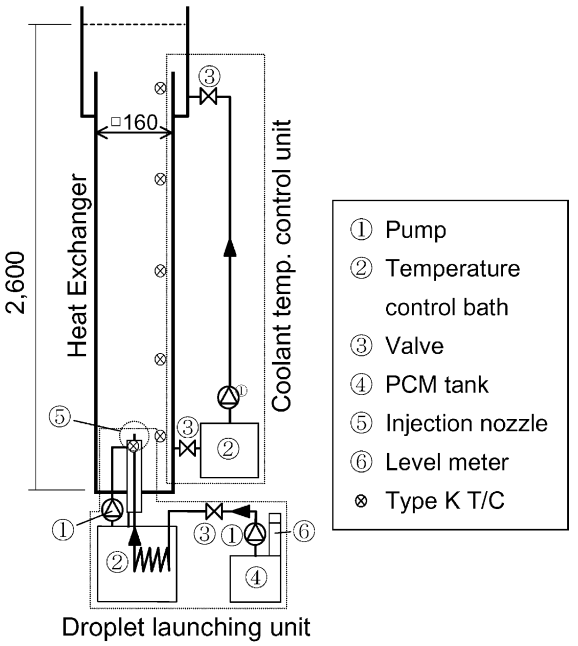

Fig. 1. Experimental heat exchange apparatus.

Table 1
Physical property of hexadecane and coolants

Hexadecane			
Latent heat (kJ/kg)	228.8		
Melting point (°C)	18.2		
	Liq. (20 °C)	Sol. (5 °C)	
Density (kg/m^3)	773	820	
Specific heat (kJ/kg K)	2.0	1.8	
Thermal conductivity (W/m K)	0.169	0.337	
	EG 0 wt%	EG 30 wt%	EG 50 wt%
Coolant			
Density (kg/m^3)	999.8	1042	1072
	999.5	1040.3	1070
Dynamic viscosity (cSt)	1.35	2.90	5.10
	1.23	2.57	4.29
Specific heat (kJ/kg K)	4.19	3.82	3.50
	4.19	3.83	3.52
Thermal conductivity (W/m K)	0.580	0.456	0.383
	0.586	0.457	0.384

In ethylene glycol water solution, upper values are measured at 9.0 °C, and lower values are measured at 12.3 °C.

the temperature of the injected hexadecane. The hexadecane injection rate is determined by readings from the liquid level meter in the PCM tank in the droplet-launching unit.

Using a video camera, we recorded the formation pattern of hexadecane droplets at the injection nozzle exit and their rising motions in the coolant. The shape, diameter, and rising velocity of the hexadecane droplets and particles were determined by analysis of the video recordings.

We measured the solidification mass fraction of floating particles collected from the coolant surface with a volume difference measurement device similar to the one employed by Inaba et al. [2]. The solidification mass fraction, R, of a particle was determined by Eq. (1):

$$R = \frac{M_{ps}}{M_{ptotal}} = \frac{\Delta V_{ps}}{\Delta V_{ptotal}} \tag{1}$$

where M_{ps} and M_{ptotal} are the mass of solidified portions of the collected particles and the total mass of the collected particles, respectively; and ΔV_{ps} is the volume change during the melting of the partly solidified particles. Thus, ΔV_{ps}, which corresponds to the volume change of the mass M_{ps} of the collected particles, was measured by the volume difference measurement device. ΔV_{ptotal} is the volume change corresponding to the total mass M_{ptotal} of collected particles and corresponds to the volume change of the collected particles when all particles were completely solidified. In preliminary experiments, we determined the relationship between ΔV_{ptotal} and M_{ptotal}. We also investigated the change in solidification mass fraction of particles in the vertical direction by measuring the solidification mass fraction at 100, 160, and 220 cm above the nozzle exit by adjusting the coolant depth.

The injection velocity of hexadecane was varied in the range of 0.212–1.03 m/s. The injection temperature of hexadecane was set at either 30 or 50 °C and the coolant temperature was set at either 9.0 or 12.3 °C. The corresponding dimensionless experimental parameters were varied in the particle Reynolds number range of $22.4 < Re_p < 492$, in the Prandtl number range of $8.79 < Pr < 49.9$, in the Stefan number range of $0.0475 < Ste < 0.0741$, and in the Fourier number range of $0.0566 < Fo < 1.66$.

At one experimental condition, we obtained an average particle diameter of 60–100 measured particles, an average rising velocity of 40–60 measured particles and an average solidification mass fraction of 300–2000 measured particles. These average values were used as the experimental data. Thus, we estimate the accuracies of the measured particle diameter and rising velocity to be within ±2%, and the accuracy of the solidification mass fraction within ±3.5%.

3. Formation patterns of hexadecane droplets and rising behavior of particles

It is well understood that the average droplet diameter is strongly associated with the droplet formation pattern at the injection nozzle exit. The injection velocity of liquid through the nozzle determines the formation patterns of droplets when other parameters such as the nozzle diameter, and the physical properties of the liquid PCM and coolant are fixed. Fig. 2(a) shows three typical formation patterns of hexadecane droplets. Fig. 2(b) and (c) shows the rising behavior of particles, where 50 °C hexadecane was injected into 12.3 °C EG 50 wt% water solution.

When injection velocity was low (0.212 m/s), single droplets were formed at the nozzle exit and were released at regular intervals, as shown in the left photograph of Fig. 2(a). The droplets ascended in a regular sequence in the center of the coolant tank. At intermediate injection velocity (0.484 m/s), a stable laminar-flow jet was formed at the nozzle exit. Roughly 5.0 cm above the nozzle, the laminar-flow jet regularly broke into groups of droplets having various sizes, as shown in the middle photograph of Fig. 2(a). At high injection velocity (1.03 m/s), an unstable turbulent jet was formed at the nozzle, which irregularly broke into groups of droplets having various sizes, as shown in the right photograph of Fig. 2(a). The groups of droplets generated by the separating laminar or turbulent jets dispersed in the center of the coolant tank. Initially, the larger droplets ascended in the center of the tank, and the smaller droplets ascended outside the center of the tank. The dispersal zone, however, diverged as the particles rose and approached a constant area about 100 cm above the nozzle exit.

At low injection velocity, hexadecane droplets start to solidify at almost the same height, as shown in Fig. 2(b). Deviation from the average solidification starting height was within ±2.2 cm. At intermediate and high injection velocities, the starting height of solidification deviated within ±5.0 cm. The larger solidification starting height deviation at intermediate and high injection velocities seems mainly attributable to the large deviation of the droplet sizes in these regions.

Observing the droplet formation patterns, we determined the ranges of hexadecane injection velocity for the low injection region (Region I), the intermediate injection region (Region II), and the high injection region (Region III). These velocities were less than 0.297 m/s in Region I, between 0.297 and 0.573–0.849 m/s in Region II, and greater than 0.572–0.849 m/s in Region III. The injection region boundary velocities differed with the coolant used.

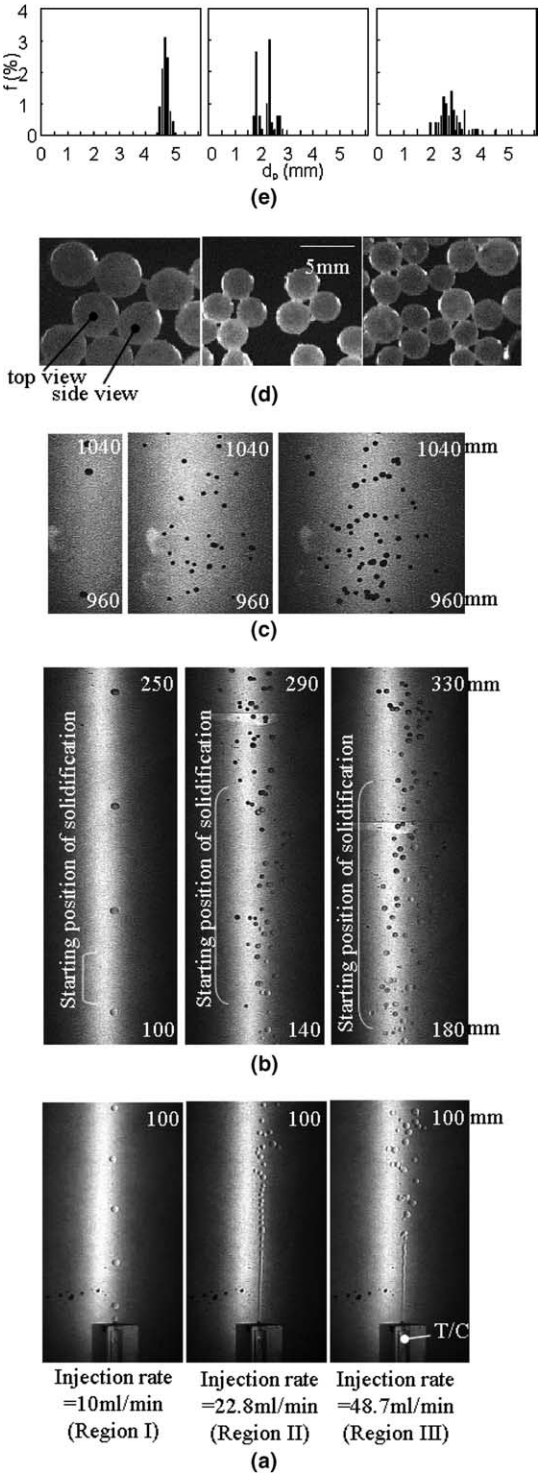

Fig. 2. Formation pattern, rising behavior, shape and diameter of particles in Regions I, II, and III (EG 50 wt% water solution, $T_n = 50$ °C, $T_c = 12.3$ °C). (a) Formation of droplets; (b) starting position of solidification; (c) rising behavior of solidified particles; (d) solidified particles; (e) distribution of average diameter of solidified particles.

4. Shape and diameter of hexadecane particles

Fig. 2(d) shows photographs of particles floating on the coolant surface. The diameters of the particles were measured using these photographs. Fig. 2(e) shows the distributions of particle diameters obtained. The particles in Region I were not exactly spherical, they were somewhat ellipsoidal in shape with a small major-to-minor diameter ratio (the diameter ratio of Region I particles in Fig. 2 was 1.25). This seems attributable to the larger average diameters of particles in Region I. The equivalent diameter d_p was calculated by Eq. (2):

$$d_p = (a^2 b)^{1/3} \tag{2}$$

where a is the major diameter and b is the minor diameter.

The equivalent diameters of Region I particles were concentrated in a narrow range, 4.5–5.1 mm, as shown in Fig. 2(e). The particles in Region II were almost spherical. The diameters of these particles were distributed in a wide range, from 1.8 to 2.9 mm. The distribution of diameters had peaks at about 1.8 and 2.3 mm, as shown in Fig. 2(e).The particles in Region III had two shapes. The smaller particles had diameters less than about 3.5 mm and were almost spherical. The larger particles had diameters greater than about 3.5 mm and were more ellipsoidal (rather than spherical), similar to the particle shapes observed in Region I. The distribution

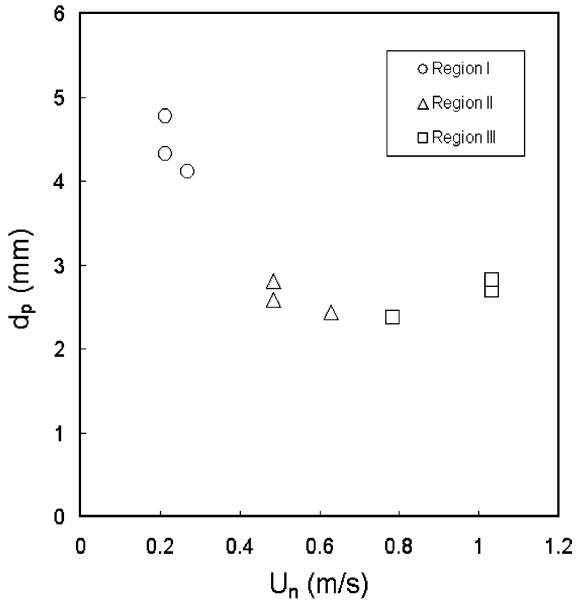

Fig. 3. Relationship between injection velocity and average diameter of particles (EG 30 wt% water solution, $T_n = 50$ °C, $T_c = 12.3$ °C).

of particle diameters had a wide range, 1.5–5.1 mm. Hence, the particles in Region II and III were mixtures of particles having various diameters.

Fig. 3 shows an example of the relationship between the injection velocity and the average diameter of particles. The average diameter in Region I decreased with an increase in the injection velocity, while the average diameters in Regions II and III remained almost constant.

In another series of similar experiments where hexadecane was injected into pure water and also into EG 30 wt% water solution, the formation patterns, rising behavior, shapes, diameters, and starting heights of droplet solidification were consistent with those described above.

5. Rising velocity and drag coefficient of hexadecane particles

Fig. 4(a) and (b) shows typical examples of 50 °C hexadecane injection into 12.3 °C EG 30 wt% water solution in Regions I, II, and III. Fig. 4(a) shows the average rising velocities of particles at various heights. Each symbol in the figure indicates the rising velocity of an average of 40–60 measured particles and the lines are calculated results that will be described later. Fig. 4(b) shows the distribution of rising velocities measured 160 cm above the injection nozzle. As a liquid droplet starts to solidify, its surface becomes enveloped by a solid layer that increases the drag coefficient of the solidifying particle as compared to that of a liquid droplet. Consequently, the rising velocity of the solidifying particle decreases gradually and asymptotically approaches the terminal rising velocity. In this experimental study, particles reached the terminal rising velocity within 100 cm above the starting height of solidification. The higher rising velocity in Region I than in Regions II and III is caused by the fact that the equivalent diameters of particles in Region I are larger than the diameters of particles in Regions II and III. The larger diameters result in stronger buoyancy. Fig. 4(b) shows that the deviation of rising velocities is small in Region I as compared with those of Regions II and III. This is mainly attributed to the smaller deviation of the particle equivalent diameters in Region I as compared with the particle diameters in Regions II and III.

Fig. 5 shows the relationship between the particle Reynolds numbers and the particle drag coefficients. Under the assumption that the rising velocities of particles had reached their terminal velocities at least 160 cm above the injection nozzle, the drag coefficients of the particles were calculated by Eq. (3):

$$C_D = \frac{4g(\rho_c - \rho_p)d_p}{3\rho_c U_{pt}^2} \tag{3}$$

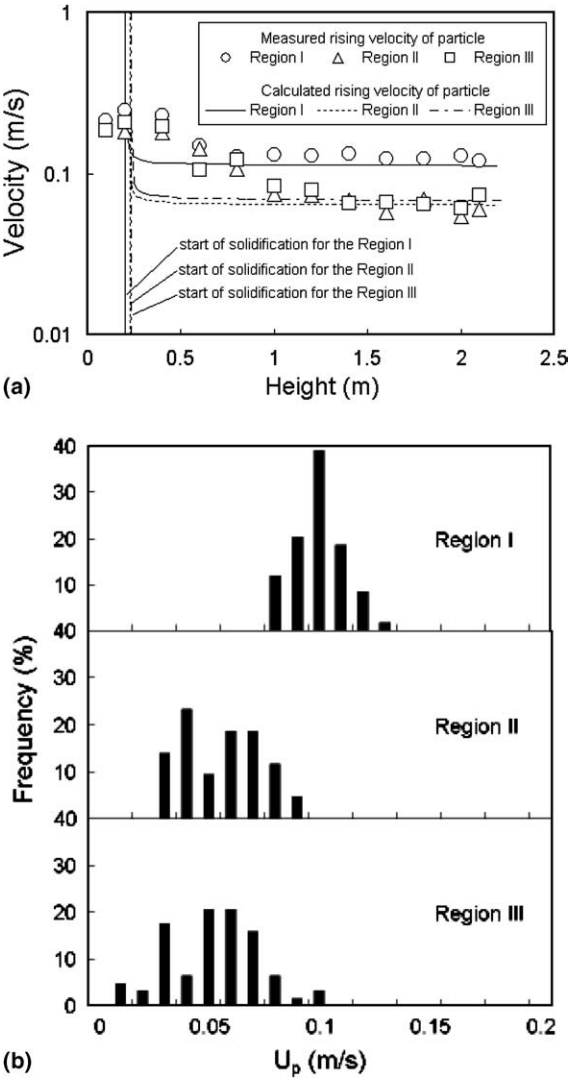

Fig. 4. (a) Measured and calculated rising velocities of particles, (b) distribution of particle velocities 160 cm above injection nozzle (EG 30 wt% water solution, T_n = 50 °C, T_c = 12.3 °C).

where U_{pt} is the rising velocity of a particle measured 160 cm above the injection nozzle. A regression curve of the experimental drag coefficients of hexadecane particles is given by empirical Eq. (4):

$$C_D = \frac{24}{Re_p}(1 + 0.15Re_p^{0.687} + 0.994Re_p^{0.296}) \tag{4}$$

Eq. (4) is plotted as the solid line in Fig. 5. For comparison, the dotted line in Fig. 5 represents the drag coefficient of the smooth solid spheres given by Eq. (5) [7]:

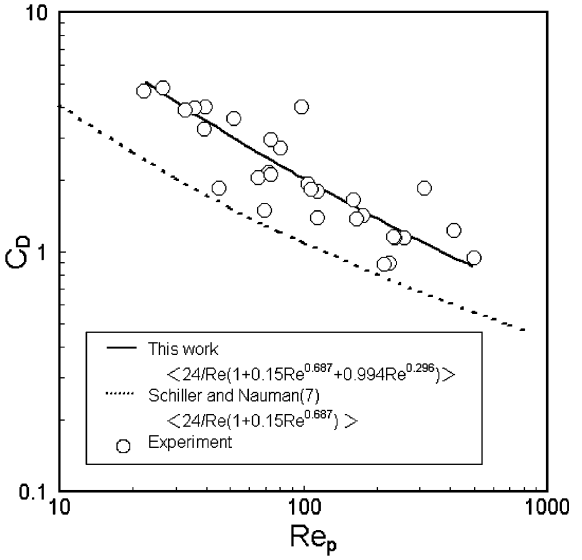

Fig. 5. Relationship between particle Reynolds numbers and drag coefficients.

$$C_D = \frac{24}{Re_p}(1 + 0.15Re^{0.687}) \tag{5}$$

Measured drag coefficients of hexadecane particles are larger than those of the smooth solid spheres estimated by Eq. (5). We hypothesize that one of the reasons for the large drag coefficient of hexadecane particles is the roughness of the solidified surface.

The symbols in Fig. 4(a) represent the experimental average rising velocities and the lines show the rising velocities calculated by the following Eq. (6) [5]:

$$\left(\rho_p + \frac{1}{2}\rho_c\right)\frac{\pi d_p^3}{6}\frac{dU_p}{dt} = (\rho_p - \rho_c)g\frac{\pi d_p^3}{6} - \rho_c\frac{\pi d_p^2}{8}C_D U_p^2 - \frac{3}{2}d_p^2\sqrt{\pi\rho_c\mu_c}\int_0^t\left(\frac{dU_p}{dt'}\right)\frac{1}{\sqrt{t-t'}}dt' \tag{6}$$

where the value of particle C_D was calculated from empirical Eq. (4), and the term $\frac{3}{2}d_p^2\sqrt{\pi\rho_c\mu_c}\int_0^t\left(\frac{dU_p}{dt'}\right)\frac{1}{\sqrt{t-t'}}dt'$ is the so-called 'Basset' term.

The calculated rising velocities decrease rapidly and approach the terminal velocities, whereas the measured rising velocities decrease gradually and approach the terminal velocities about 40–100 cm from the solidification starting height. From 40 to 100 cm above the solidification starting height, the calculated velocities are smaller than those measured.

6. Solidification mass fraction

6.1. Numerical calculation of solidification mass fraction

We calculated the temperature profile and solidification mass fraction of a droplet under the following assumptions:

(1) The particles do not interfere with one another.
(2) The heat transfer coefficient is uniform on the surface of a particle. We observed the inner shape of partially solidified particles collected from the coolant surface and found that the thickness of the solidified layer was almost uniform in a circumferential direction. The deviation from the mean thickness was within ±6%. This indicates that we can assume the heat transfer coefficient is almost uniform on the surface of a particle.
(3) The heat is transferred solely by heat conduction in a particle.
(4) The volume change by solidification is small and can be neglected, and
(5) The liquid droplets are not super-cooled.

The super-cooling degree of paraffin oils is generally small compared to other liquid like water. We measured the super-cooling degree of hexadecane by DSC (differential scanning calorimeter). It was 3.9 °C. The initial thickness of the outmost solidified layer formed by release of the 3.9 °C super-cooling is estimated to be $\ll$100 μm, which leads to the error of 10^{-12} in the solidification mass fraction. This indicates the super-cooling of liquid droplets can be neglected in the present calculation.

Under these assumptions, the temperature profile within a particle was calculated by solving the following one-dimensional, non-steady-state, heat conduction equation:

$$\frac{\partial H}{\partial t} = \frac{1}{r^2}\frac{\partial}{\partial r}\left(r^2\lambda\frac{\partial T}{\partial r}\right) \tag{7}$$

$$H = \rho cT + (1-\gamma)\rho L \tag{8}$$

The boundary and initial conditions are given by:

$$(1)\ \text{at } r = 0, \quad \frac{\partial T}{\partial r} = 0 \tag{9}$$

$$(2)\ \text{at } r = r_0, \quad -\lambda\frac{\partial T}{\partial r} = h(T_0 - T_c) \tag{10}$$

$$(3)\ \text{at } t = 0, \quad r = 0\text{–}r_0, \quad T = T_n \tag{11}$$

The heat transfer coefficient h on the surface of a liquid droplet was calculated from an empirical relationship proposed by Conkie and Savic [8] (Eq. (12)):

$$Nu_{lo} = 2 + 0.90Re^{0.5} \cdot Pr^{0.5} \quad (12)$$

and that for a solidified particle was determined from an empirical equation of Nu for a rigid particle proposed by Tsubouchi and Masuda [9] (Eq. (13)):

$$Nu_{so} = 2 + 0.57Re^{0.5} \cdot Pr^{1/3} \quad (13)$$

The temperature dependence of the physical properties was considered in the above calculations.

The lines in Fig. 6 represent calculated temperature distributions within particles rising in pure water. The injection temperature of hexadecane was $T_n = 50$ °C, the coolant temperature was $T_c = 9$ °C, the injection velocity was 0.212 m/s (10 ml/min), and the droplet diameter was 4.32 mm. The calculated temperature distribution in a liquid droplet indicates that the starting time of solidification was about 0.5 s whereas the measured one was about 1.5–3 s. This difference seems to indicate that the temperature distribution in a liquid droplet before solidification is rather difficult to predict by the one-dimensional heat conduction model, because (1) an internal circulation flow might exist in a droplet and (2) heat transfer during the formation process of particle at an injection nozzle is difficult to predict.

It seems, however, we can predict the temperature distribution in a solid layer during the solidification process, because we can neglect the heat transfer in the central liquid part of a particle during the solidification period. The reasons for this are (1) the main heat resistance in the particle is the solidified layer and (2) sensible heat release rate from the liquid core is negligibly small compared to latent heat release rate at the interface between the solid layer and the liquid core, as will be explained in Section 6.2.

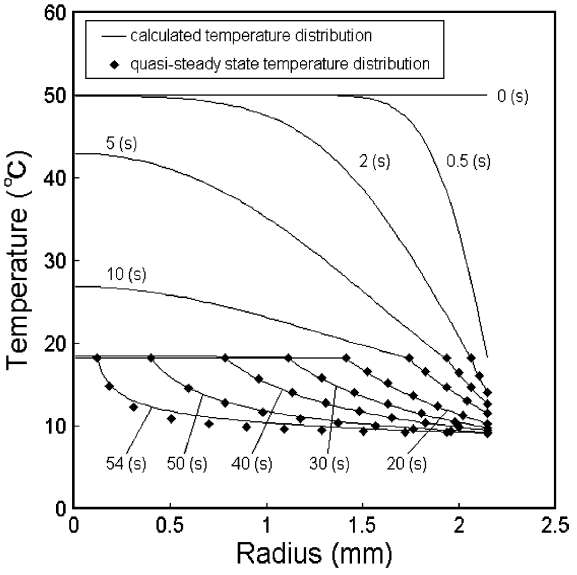

Fig. 6. Radius vs. temperature distributions in rising particles.

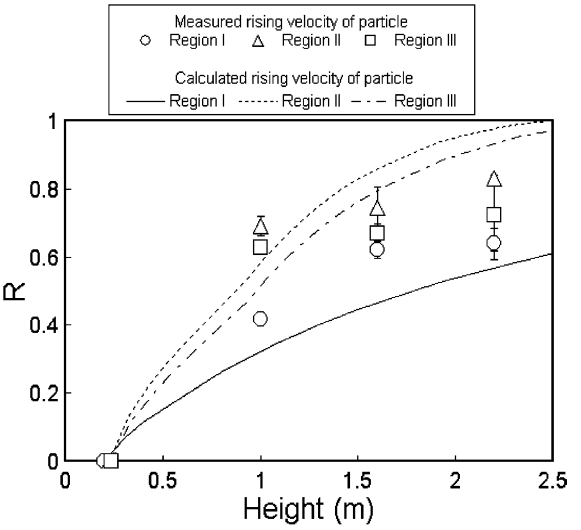

Fig. 7. Comparison of measured and calculated solidification mass fractions (EG 30 wt% water solution, $T_n = 50$ °C, $T_c = 12.3$ °C).

Fig. 7 shows a comparison of calculated and measured solidification mass fraction profiles in Regions I, II, and III. The solidification mass fractions were determined from the calculated temperature distributions in the solid layer. The symbols represent experimental data measured at locations 100, 160, and 220 cm above the nozzle exit, and the lines are the calculated profiles. We plotted the calculated solidification mass fraction profiles so that the starting locations of solidification fell on the same positions as those measured. Fig. 8 shows comparisons of the calculated and measured solidification mass fractions for the present experimental conditions. In Region I, the calculated mass fraction values are less than those measured. The shapes of solidification mass fraction profiles, however, are rather similar to each other as shown in Fig. 7. This difference in the solidification mass fraction values seems to be attributed to the fact that the Nusselt number of the solidified particles used in this experimental study is higher than that of a solid particle given by Eq. (13). It is possible that the heat transfer coefficient of Region I solidified particles is larger than that of the rigid particles, because the shape of particle in Region I is ellipsoidal. On the other hand, the calculated solidification mass fractions are quite different from those measured in Regions II and III. These differences seem to be caused by the interference of neighboring particles.

Comparing the measured solidification mass fractions of particles ascending in low temperature coolant

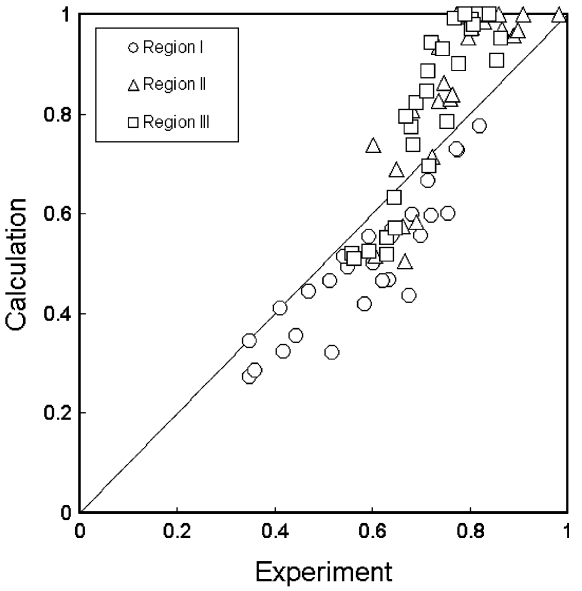

Fig. 8. Comparison of measured and calculated solidification mass fractions.

(9 °C) with those in high temperature coolant (12.3 °C), we found that in injection Region I, the lower the coolant temperature, the higher the solidification mass fraction becomes. That is, Region I particles ascending in low temperature coolant (9 °C) have a larger solidification mass fraction compared to those in high temperature coolant (12.3 °C). On the other hand, in Regions II and III, the particles ascending in low (9 °C) and high (12.3 °C) temperature coolants have almost the same solidification mass fractions. In other words, the solidification mass fractions of the particles in Regions II and III are not affected by bulk coolant temperature. This seems to indicate that Regions II and III particle heat transfer coefficients are quite different from that of a single particle due to interference among particles. It seems this caused the differences between the measured and calculated solidification mass fractions in Regions II and III in Fig. 8. The effect of the interaction among particles on the heat transfer will be discussed in the next section.

In order to investigate the effect of temperature profile in the center liquid core on the solidification rate, we calculated the solidification mass fraction of a particle with a hypothesis that the center liquid core has a uniform temperature (melting temperature). The calculated solidification mass fraction under this hypothesis agreed well with the solidification curve in Fig. 7 within ±1.6%. (Note that the solidification curve in Fig. 7 was calculated for a particle with the liquid core temperature distribution shown in Fig. 6.) This indicates that the temperature distribution in center liquid core is of little importance for the calculation of solidification mass fraction.

If the completion time for complete solidification of hexadecane droplets injected into water of 12.3 °C coolant is calculated by the present numerical method, it is estimated to be about 12 s or 0.66 m above the starting position of solidification for the particle with 1.7 mm diameter, about 50 s or 5.0 m for the particle with 3.5 mm diameter and about 100 s or 14 m for the particle with 5.0 mm diameter. As the ethylene glycol concentration in the coolant becomes larger, the completion time increases.

6.2. Empirical relationship for solidification mass fractions in Regions I, II, and III

Fig. 6 shows a comparison of temperature distributions in a growing solid layer in a particle. The solid lines are the non-steady-state temperature distributions calculated by Eq. (7), and the symbols represent the quasi-steady-state temperature distributions calculated by Eq. (14):

$$T = T_{\mathrm{i}} - \left(\frac{T_{\mathrm{i}} - T_{\mathrm{o}}}{\dfrac{1}{r_{\mathrm{i}}} - \dfrac{1}{r_{\mathrm{o}}}}\right)\left(\frac{1}{r_{\mathrm{i}}} - \frac{1}{r}\right) \tag{14}$$

where T_{i} (= melting temperature of hexadecane) and T_{o} are the inner and outer surface temperature of the solid envelope, respectively. As shown in Fig. 6, the quasi-steady-state temperature distributions calculated by Eq. (14) agree well with the numerically calculated non-steady-state temperature distributions.

Fig. 9 shows the ratio of the sensible heat release rate to the total heat release rate (sensible heat + latent heat).

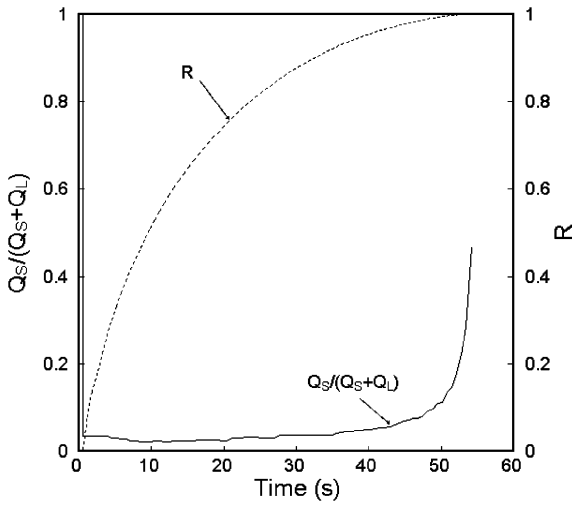

Fig. 9. Ratio of sensible heat release rate to total heat release rate with time.

Except during the initial very short period and in the last seconds, it is obvious that the sensible heat release rate is negligibly small compared to the latent heat release rate that occurs during the long intermediate period relevant to the solidification process. In the initial very short period, the ratio is large because the sensible heat release rate is large. This is caused by the large temperature gradient that exists in the liquid hexadecane. In the last period when the solidification mass fraction approaches 1 (after about 80–90 s), the ratio $(Q_S/(Q_S + Q_L))$ also becomes large because during this period of solidification the latent heat release rate from the shrinking liquid core approaches zero. Thus, the first and last periods of solidification are of minimal importance to the total heat transfer during the aggregate solidification process because they are of very short durations.

Under the above mentioned assumptions, that is, (1) the temperature distribution in the solidified layer in a particle is represented well by a quasi-steady-state temperature distribution, (2) the sensible heat release in the liquid core of a particle is negligibly small compared to the latent heat release rate, the continuity equation for energy at the liquid–solid interface in the particle where solidification is taking place is expressed by Eq. (15):

$$-\rho_{ps}\cdot L\cdot 4\pi r_i^2\cdot dr_i = -\lambda_{ps}\left(\frac{\partial T}{\partial r}\right)_{r=r_i} 4\pi r_i^2\cdot dt = 4\pi r_o^2(T_m - T_c)\frac{1}{\frac{1}{h}+\frac{r_o^2}{\lambda_{ps}\cdot r_i}-\frac{r_o}{\lambda_{ps}}}dt \tag{15}$$

where the value of h is approximately 10^3–10^4 W/(m^{2}K). By introducing dimensionless radius $r_i^* = r_i/r_o$ and time $t^* = t/t_f$ into Eq. (15), we obtain Eq. (16):

$$(r_i^*)^2\left(\frac{dr_i^*}{dt^*}\right) = -4(Ste\cdot Fo)\cdot\frac{1}{\frac{2}{Bi}+\frac{1}{r_i^*}-1} \tag{16}$$

and the solidification mass fraction R defined by Eq. (1) becomes Eq. (17):

$$R = \frac{1-(r_i^*)^3}{1-(1-\rho^*)(r_i^*)^3} \tag{17}$$

where $(\rho^* = \frac{\rho_{pl}}{\rho_{ps}})$ is constant in this study, and t_f is the time required for a particle to reach the top surface of the coolant from the starting height of solidification.

Substituting Eq. (17) into Eq. (16), we obtain Eq. (18):

$$\frac{dR}{dt^*} = 12\frac{(Ste\cdot Fo)}{\rho^*}\cdot\frac{\{1+R(\rho^*-1)\}^2}{\frac{2}{Bi}+\left\{\frac{1+R(\rho^*-1)}{1-R}\right\}^{\frac{1}{3}}-1} \tag{18}$$

Eq. (18) indicates that the solidification mass fraction R is a function of $(Ste\cdot Fo)$, Bi, and ρ^*. Since $Bi = Nu\times(\lambda^* = \frac{\lambda_c}{\lambda_{ps}}) = Nu\times\lambda^*$, we obtain Eq. (19):

$$R = f[(Ste\cdot Fo),(Nu\cdot\lambda^*),\rho^*] \tag{19}$$

Nakao et al. [10] found that Nusselt number of particles in a swarm of spherical particles with the same diameter can be expressed by a correlation Nu = (constant) × Nu_{so}, where Nu_{so} is Nusselt number for a solid particle and (constant) has different value according to the particle density defined by $n = N/(A\cdot U_p)$. Where N is the number of particles, and A is area of the cross section of coolant tank. Their experimental results indicated that (constant) is 1.0 when the particle density is below 0.01, and it is about 0.3 when the particle density is above 0.1. As the correlation $Nu_{so} = 2 + 0.57Re^{0.5}\cdot Pr^{1/3}$ proposed by Tubouchi and Masuda [9] is approximated by $Nu = 0.62\times Re^{0.5}\cdot Pr^{1/3}$ in our experimental conditions, it may be possible to postulate $Nu = C\times Re_p^{0.5}\times Pr^{1/3}$ for particles used in the present experiments. The constant C, however, have different values for the particles in the Region I where the particle density is about 0.001 and for the particles in the Regions II and III where the particle density is about 0.1. The constant C may have different values from those values proposed by Nakao et al., as the present particle swarms contain sphere and elliptic particles. Strictly speaking, exponents of Re_p and Pr might be different from 0.5 and 1/3, however, it may be possible to postulate $Nu = C\times Re_p^{0.5}\times Pr^{1/3}$, because the major-to-minor diameter ratio is less than 1.25 in the present experiment. Substituting the postulated correlation for Nusselt number into Eq. (19), we get Eq. (20):

$$R = f[(Ste\cdot Fo),(Re_p^{0.5}\cdot Pr^{1/3}\cdot\lambda^*),\rho^*] \tag{20}$$

Following dimensionless analysis methodology, we can assume R is proportional to the products of power functions of independent variables. Eq. (20) then becomes Eq. (21):

$$R = C\cdot(Ste\cdot Fo)^{c,}(Re_p^{0.5}\cdot Pr^{1/3}\cdot\lambda^*)^d = C\cdot(Ste\cdot Fo)^{k,}Re_p^l\cdot Pr^m\cdot(\lambda^*)^n \tag{21}$$

Note that ρ^* is omitted in Eq. (21) because it remained constant in this study. The proportional constant C and the power exponents of k, l, m, and n are determined from experimental data by the least-squares method. Thus, we propose the following equations for the solidification mass fraction. As the particles in Region I and the particles in Regions II and III have different profiles of solidification mass fraction, we propose two empirical expressions, Eqs. (22) and (23):

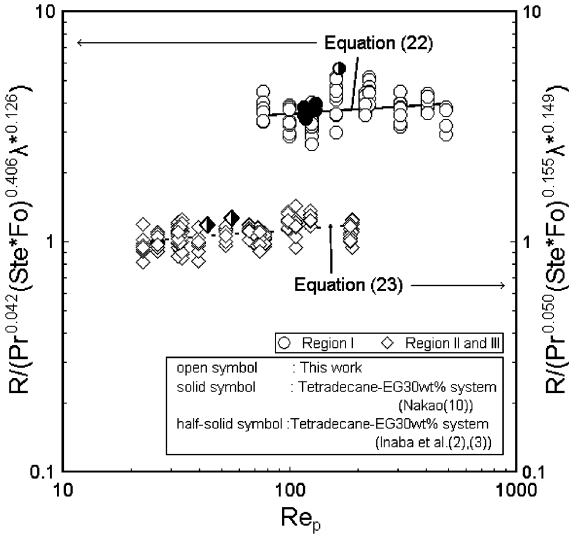

Fig. 10. Comparison of empirical expressions for the solidification mass fraction with measured data.

$$R = 2.69 Re_p^{0.063} Pr^{0.042} (Ste \cdot Fo)^{0.406} \lambda^{*0.126}$$
$$\left(\begin{array}{l} \text{Region I}: \ 76.3 \leqslant Re_p \leqslant 492, \ 8.79 \leqslant Pr \leqslant 49.9, \\ 0.0475 \leqslant Ste \leqslant 0.074, \ 0.056 \leqslant Fo \leqslant 0.221, \\ 1.15 \leqslant \lambda^* \leqslant 1.75 \end{array} \right) \quad (22)$$

$$R = 0.796 Re_p^{0.075} Pr^{0.050} (Ste \cdot Fo)^{0.155} \lambda^{*0.149}$$
$$\left(\begin{array}{l} \text{Region II and III}: \ 22.4 \leqslant Re_p \leqslant 187, \ 8.79 \leqslant Pr \leqslant 49.9, \\ 0.0475 \leqslant Ste \leqslant 0.0741, \ 0.144 \leqslant Fo \leqslant 1.66, \\ 1.15 \leqslant \lambda^* \leqslant 1.75 \end{array} \right) \quad (23)$$

Fig. 10 is a comparison of the dimensionless expressions and experimental data. In this figure, solidification mass fractions R of tetradecane injected into EG 30 wt% water solution are also plotted for reference purposes. These experimental data were measured by Inaba et al. [4] and Nakao et al. [11] in a tetradecane-EG 30 wt% water solution experimental system. These experimental data for tetradecane also correlate well with empirical Eqs. (22) and (23) above.

7. Conclusions

Solidification characteristics of hexadecane particles injected through a single nozzle into coolants of stagnant pure water, ethylene glycol 30 wt% water solution, and ethylene glycol 50 wt% water solution were investigated. Experimental parameters were varied in the ranges of $22.4 < Re_p < 492$, $8.79 < Pr < 49.9$, $0.0475 < Ste < 0.0741$, and $0.0566 < Fo < 1.66$. The present study focused on the solidification phenomena in the second step of the heat transfer process.

The following conclusions were derived from the present study.

(1) The empirical equation correlating the drag coefficients of hexadecane particles was proposed.
(2) The empirical equations correlating the solidification mass fractions of hexadecane particles were proposed for injection Region I and for injection Regions II and III.

References

[1] T. Shirotuka et al., SCEJ 31 (1967) 425.
[2] H. Inaba et al., Trans. JSME(B) 60 (580) (1994) 4236–4243.
[3] H. Inaba et al., Trans. JSME(B) 62 (593) (1996) 325–332.
[4] H. Inaba et al., Trans. JSME(B) 63 (607) (1997) 1013–1020.
[5] J.Q. Hinze, Turbulence, second ed., McGraw Hill, 1975, pp. 352–364.
[6] H. Inaba et al., Trans. JSME(B) 65 (635) (1999) 2454–2461.
[7] L. Schiller, A.Z. Nauman, Ver. Deut. Ing 77 (1933) 318–320.
[8] W.R. Conkie, P. Savic, National Research Council of Canada, Div. Mech. Engng., Report MT-23, 1953.
[9] T. Tsubouchi, H. Masuda, Trans. JSME(B) 30 (219) (1994) 1394–1401.
[10] Y. Nakao et al., in: Proceedings of the 2003 JSRAE Annual Conference, Kanazawa, Japan.
[11] Y. Nakao et al., The Fifth JSME-KSME Fluids Engineering Conference, Nagoya, Japan, 2002.